ADVANCED MATERIALS INTERFACES
www.advmatinterfaces.de

pH-Responsive Motors and their Interaction with RAW 264.7 Macrophages

*Miguel A. Ramos Docampo, Xiaomin Qian, Carina Ade, Thaís Floriano Marcelino, Marcel Ceccato, Morten Foss, Ondrej Hovorka, and Brigitte Städler**

Nano/micromotors are self-propelled particles that use external stimuli to gain locomotion outperforming Brownian motion. Here, three different polymers are employed that are conjugated to silica particles through a pH-labile linker. At slightly acidic pH, the linkers hydrolyze and release the polymeric chains, resulting in enhanced locomotion. The motors show a maximum velocity of ≈3 µm s^{-1} in cell media when poly(ethylene glycol) methyl ether methacrylate is asymmetrically distributed on the surface of the particles. Further, the motor internalization by RAW 264.7 macrophages was compared between motors, which have the polymer conjugated via a pH-labile linker, and the irresponsive particles. Preliminary data indicate enhanced uptake, but further efforts are required to use responsive polymers to propel motors inside mammalian cells.

1. Introduction

Nano- and micromotors are small objects that are able to convert different types of energy into kinetic energy and mechanical power to exhibit (self-propelled) locomotion. Different concepts of autonomous motion and their potential applications were recently outlined in detail in several reviews.[1–4] Application of these motors in biomedicine requires non-cytotoxic building blocks as well as bio-friendly fuels and combustion products, or physical stimuli that are harmless for cells and tissues. Exploring the benefit of motors over their passively diffusing counterparts in cell culture or in animal models attracted substantial attention in the past years.[5,6] Early examples focused on externally-driven motors that made use of physical stimuli to propel in low-density media. Recent examples include the use of near-infrared (NIR) light-activated motors to penetrate a 3D cell tumor culture, which selectively induced cell apoptosis upon NIR irradiation or resulted in depleted amyloid aggregation.[7] Similarly, magnetically driven motors made of $CaCO_3$ and Fe_3O_4 showed an increased cellular uptake since their mobility allowed for more efficient approaching of the target area.[8] The decomposition of the core particle in the acidic environment of the lysosomes assisted cargo release. In a different approach, Shen et al. employed Zn-doped iron oxide rods that swarmed and eventually spun under a rotating magnetic field, inducing cell death.[9] This effect was also assessed in vivo, where the size of tumors generated in mice decreased 4× upon magnetic therapy. Further, ultrasound-powered motors used for antigen delivery showed a 5–7-fold increase in cell penetration compared to passive particles.[10]

Alternatively, motors that harvest energy from their local environment are a powerful option to design truly autonomous motors. There are examples of motors that showed locomotion in simple 2D cell models as well as more complex 3D cultures and even in animal models. Mesoporous silica particles[11] or liposomes[12,13] were chosen to assess cellular uptake in 2D cultures, showing promising results. For instance, Llopis-Lorente et al. engineered a mesoporous silica motor that moved due to the conversion of urea into ammonia and CO_2.[14] After entrapment in the lysosomes, a 4× lower motor concentration was needed to release the same amount of cargo as their passive particle counterparts, an aspect that was attributed to the enhanced diffusion of the motors. Further, Wilson and co-workers designed a drug-loaded liposome-based motor that gained locomotion in the acidic pH generated in the surroundings of HeLa cells.[15] These motors showed a chemotactic behavior towards acidic environments where they reached speeds up to ≈9 µm s^{-1} at pH 4.6.

Other motors were able to penetrate 3D cell environments or tissues. For example, we showed that collagenase-propelled motors posed velocities up to 22 µm s^{-1} in collagen fiber networks, being eventually able to enhance penetration into bone

---

M. A. Ramos Docampo, X. Qian, C. Ade, T. Floriano Marcelino,
M. Ceccato, M. Foss, B. Städler
Interdisciplinary Nanoscience Center (iNANO)
Aarhus University
Gustav Wieds Vej 14, Aarhus 8000, Denmark
E-mail: bstadler@inano.au.dk

T. Floriano Marcelino
Sino-Danish Center for Education and Research (SDC)
University of Chinese Academy of Sciences
China

O. Hovorka
Faculty of Engineering and Physical Sciences
University of Southampton
Southampton SO16 7QF, UK

The ORCID identification number(s) for the author(s) of this article can be found under https://doi.org/10.1002/admi.202201509.

DOI: 10.1002/admi.202201509

cell spheroids compared to the passive controls.[16] Similarly, Hortelão and co-workers showed that urea-powered motors were able to enter bladder cancer spheroids and impair the cell viability.[17] Alternatively, motors that employ manganese oxide indicated increased uptake by cells in both 2D and 3D cultures.[18] These motors moved up to ≈6 µm s^{-1} in 50 mM H_2O_2, and facilitated the production of hydroxyl radicals by consuming overexpressed glutathione and thus, contributed to intracellular chemodynamic therapy. From a different perspective, efficient lysosomal escape strategies remain a challenge in nanomedicine. Current efforts included the use of polycation transfection,[19] virus-mimicking particles,[20] cell-penetrating peptides,[21] and pH-responsive moieties.[22,23] Motors have also been considered in this context, for example, Gisbert-Garzarán et al. have employed silica particles conjugated to a polymer through a redox-responsive linker that showed indications of lysosomal escape abilities.[24]

Motors were also explored in animal models. Xu et al. used magnesium oxide motors to scavenge hydroxyl radicals and produce hydrogen, which would alleviate arthritis inflammation.[25] These motors showed long linear trajectories in buffer that became circular in simulated synovial fluid with comparable velocities up to 40–45 µm s^{-1} in both environments. When injected into diseased rats, the motors' performance could alleviate the inflammation and cartilage erosion with negligible hemolysis. Another elegant strategy utilized bottle-like inorganic motors to neutralize gastric acid and treat *Helicobacter pylori* infections.[5] The motors moved at an average speed of 40 µm s^{-1} in simulated gastric acid (pH = 1.3) and when 15 mg of the motors were internalized in gastric acid tissue, they could equilibrate the pH within 10 min without being considered toxic. Mice affected by *Helicobacter pylori* had a threefold decrease in the bacteria colonies after 5 days of treatment.

Herein, we explore the locomotion of motors with conjugated polymer chains via a pH-responsive linker and their interaction with RAW 264.7 macrophages focusing on uptake efficacy and intracellular location. Specifically, we i) compared the stability of two acid-labile linkers followed by their conjugation to poly(hydroxyethyl methacrylate) (PHEMA), poly(2-carboxyethyl acrylate) (PCEA), and poly(ethylene glycol) methyl ether methacrylate (PEGMA), ii) assessed the modification of planar and colloidal surfaces with these polymers, and monitored the pH-triggered detachment of the polymer chains, iii) evaluated the locomotion properties of these polymer-coated motors, and iv) incubated the lead motor in RAW 264.7 macrophages to compare uptake efficacy and intracellular location to irresponsive particles (**Scheme 1**).

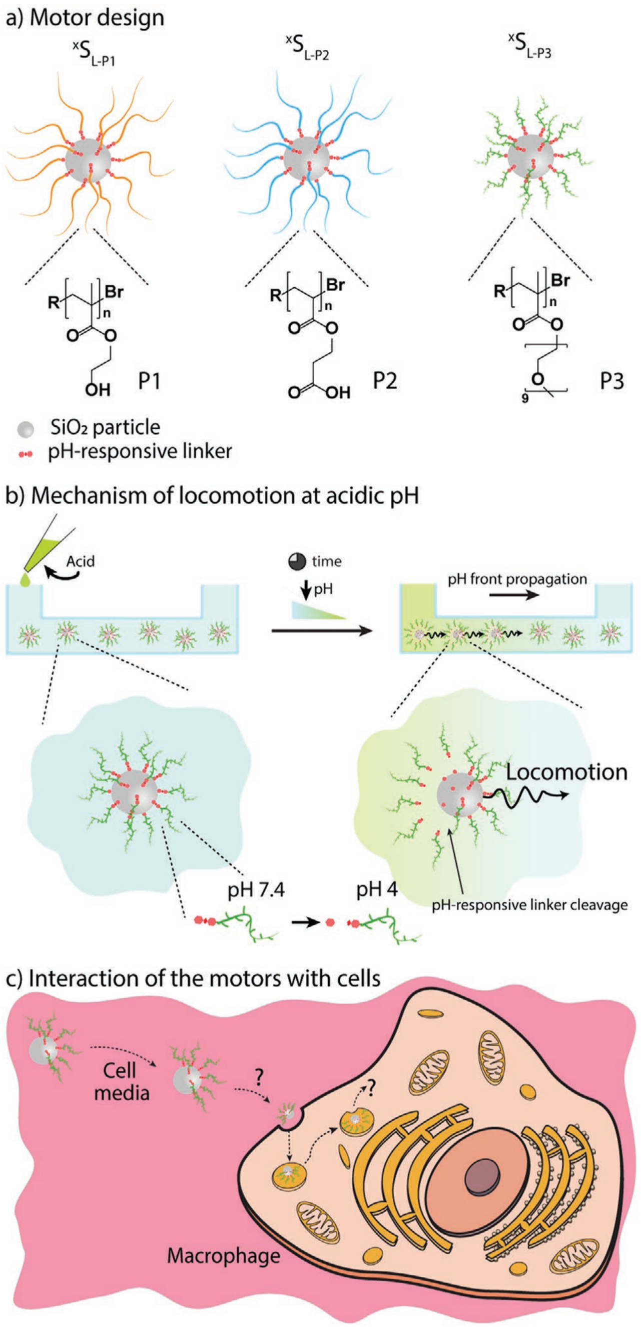

Scheme 1. a) Cartoons depicting the three types of motors coated with PHEMA (P1), PCEA (P2), and PEGMA (P3) via a pH-labile linker. b) Cleavage of the pH-responsive linker upon decreasing the pH of the medium, which results in the locomotion of the motor. c) Biological evaluation of the motors and their intracellular fate in RAW 264.7 macrophages.

2. Results and Discussion

2.1. Design of Acid-Labile Linkers

Acid-labile linkers are an interesting means to make polymers responsive to pH changes in their environment and have been widely explored in drug delivery as discussed in detail in several recent reviews.[26–28] We chose to use an imine bond as the acid labile group. Imine is a dynamic covalent bond that can be easily prepared from the condensation reaction of an amine and a carbonyl (e.g., aldehyde), which is an equilibrium process that can be driven to the starting materials at low pH (**Figure 1**a). This dynamic process has been used extensively to prepare acid-responsive biomaterials.[29–32] The sensitivity of imine to acidic pH can be tuned by carefully choosing the types of amine and aldehyde. We synthesized two acid-labile linkers L_1 and L_2, and a control linker L_0 that had no imine group (Figure 1b). On a molecular level, L_2 possessed an extra phenyl ring compared to

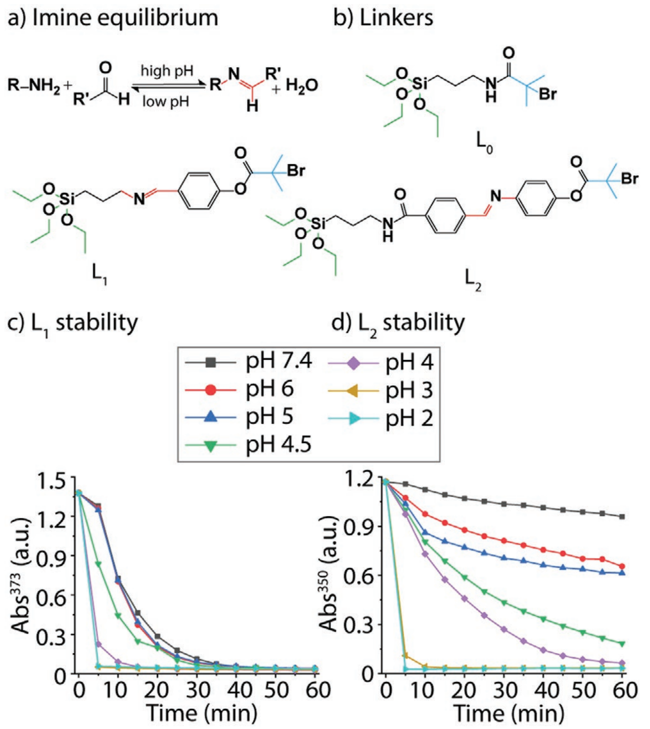

Figure 1. Acid-labile linkers. a) The dynamic equilibrium of the formation and disassociation of imine at high and low pH. b) Chemical structures of linker L_0, L_1, and L_2. c,d) The time-dependent (1 h, time interval $\Delta t = 5$ min) absorbance of the π-π^* transition of the C=N group in L_1 and L_2 at different pH ($n = 1$).

L_1, which was anticipated to improve the stability against acidic decomposition. Previously, it has been reported that imines could be stabilized through π-π conjugation between aromatic substituents and C=N bonds.[33]

We first compared the stability of L_1 and L_2 by monitoring the time-dependent absorption of both linkers at pH between 2 and 7.4. The peak at $\lambda_{ab} = 373$ nm, corresponding to the π-π^* transition of the C=N group, decreased over time even at neutral pH for L_1, reaching the baseline value after 30 min. L_1 disintegrated within minutes when exposed to pH 4 and below (Figure 1c). L_2, on the other hand, showed the expected improved stability at neutral pH as the absorbance only decreased by 0.1 units in 1 h (Figure 1d). The most dominant change in hydrolysis speed took place between pH 5 to 4. Almost complete hydrolysis of L_2 was observed at pH 4 within 50 min. L_2 was chosen as the acid-labile linker for further studies since it showed improved stability at neutral pH compared to L_1, and it had efficient hydrolysis in a pH range relevant for lysosomal escape.

2.2. Polymer Synthesis

Next, atom transfer radical polymerization (ATRP) was conducted using L_0 or L_2 as the initiator and either 2-hydroxyethyl methacrylate (HEMA), 2-carboxyethyl acrylate (CEA), or poly(ethylene glycol) methyl ether methacrylate (PEGMA, average Mn = 500 Da) as the monomer. HEMA was chosen as the monomer since PHEMA is a well-explored biocompatible polymer that has found extensive biomedical applications.[34,35] CEA results in a pH-sensitive polyanion with low cytotoxicity,[36] which we previously used as the hydrophilic block in block copolymers to prepare micelles or hybrid vesicles.[37,38] PEGMA is a water-soluble, biocompatible polymer that has found enormous applications in bioconjugation,[39] drug delivery,[27] and bioengineering.[40]

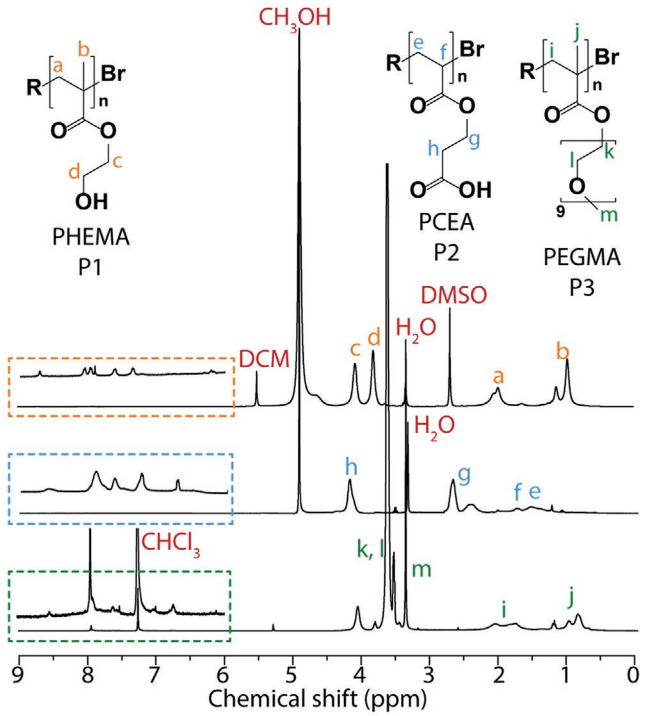

Figure 2. ^{1}H-NMR spectra (400 MHz) of P1 (CD_3OD), P2 (CD_3OD), and P3 ($CDCl_3$) synthesized via ATRP using L_2 as the initiator with 1 h reaction time. The insets show a close-up of the aromatic region, in which the signals were attributed to the benzene rings on L_2.

The polymerization was done with a typical ATRP procedure in DMSO resulting in P1, P2, and P3 when using HEMA, CEA, and PEGMA, respectively, as the monomer. Each polymer was synthesized using either L_0 or L_2 as the initiator (e.g., P1 (when using L_0) or L-P1 where L indicates the use of the pH-responsive linker L_2). Each polymer was synthesized with two different reaction times resulting in low molecular weight polymers (e.g., $P1_S$) or high molecular weight polymers (e.g., $P1_L$) to investigate the influence of the polymer chain molecular weight on the locomotion properties.

The successful polymerization using HEMA was confirmed by ^{1}H-NMR (**Figure 2**). The broad peaks of the methyl group (peak b) and the methylene group (peak a) on the backbone were seen around 1 and 2 ppm, respectively, while the two broad peaks around 3.8 ppm (peak d) and 4.1 ppm (peak c) were attributed to the side chains. The aromatic proton signals of L_2 could also be observed in the down field (6–9 ppm). The reaction time showed a clear influence on the molecular weight of P1. $P1_S$ and $P1_L$ with 20–25 (≈3 kDa, 1 h polymerization) and 60–67 (≈8.5 kDa, 24 h polymerization) repeating units, respectively, were obtained.

The successful polymer synthesis using CEA with L_0 or L_2 as the initiator was confirmed by ^{1}H-NMR as indicated by the presence of the polymer backbone protons (peaks e and f), the side chain protons (peaks g and h), as well as the aromatic protons in the downfield (6–9 ppm). P2 or L-P2 (where L indicates the use of the pH-responsive linker L_2) with 24–32 repeating units (≈4 kDa) were obtained for a 1 h reaction time, or with 48–60 repeating units (≈8 kDa) while 24 h reaction time was allowed.

Finally, we prepared the polymer PEGMA using L_0 or L_2 as the initiator and poly(ethylene glycol) methyl ether methacrylate (average Mn = 500 Da, which corresponds to 9 repeating units) as the monomer. The existence of the protons on the PEG side chain (peaks k, l, and m) and on the backbone (peaks i and j) in the ^{1}H-NMR spectrum indicated the successful polymerization. 1 h reaction time typically gave 16–20 repeating units (≈2.3 kDa) for $P3_S$ or L-$P3_S$ while 5 h reaction time gave 36–45 repeating units (≈5.5 kDa) for $P3_L$ or L-$P3_L$.

2.3. Polymer Coatings on Planar Surfaces

With the aim to evaluate the possibility to cleave the polymer from a solid support upon acidification of the environment, silica wafers were coated and incubated at either pH 7.4 or pH 4.0 for 2 h and analyzed using X-ray photoemission spectroscopy (XPS). $P1_{S/L}$ and L-$P1_{S/L}$ were chosen as representative examples. The atomic percentage of Si, C, O, and N was determined based on the peak areas in every sample (**Table 1** and Table S1, Supporting Information). First, the increasing percentages of C, O, and N confirmed the deposition of all four polymers on the silica surfaces. Second, samples coated with $P1_S$ and $P1_L$ had a C/Si ratio of 1.7–2.9 independent of the exposure to acidic pH, illustrating an irresponsive polymer coating. In contrast, the atomic ratio C/Si was calculated to be 1.7–1.8 for L-$P1_S$ and L-$P1_L$ incubated at pH 7.4, while it dropped to 1.0–1.1 when incubated at pH 4, indicating the expected detachment of the polymer chains from the surface.

2.4. Coatings on Colloids

Silica (SiO_2) particles were synthesized by a modified Stöber method, which uses the hydrolysis and condensation of the silica precursor (i.e., TEOS or APTES) assisted by an alkaline catalyst (i.e., NH_4OH). The synthesis was tuned to obtain sub-100 and 500 nm SiO_2 particles for the cell interaction studies and the locomotion analysis using optical microscopy, respectively. Specifically, SiO_2 particles with an average diameter of 75 (±14) nm and 510 (±68) nm (Gaussian distribution, for 95.5% of the population), respectively, were obtained as determined from electron microscopy (EM) images (Figure S1, Supporting Information). The SiO_2 particles will be referred to as ^{x}S from now where x indicates their diameter in nm. Fluorescently labeled SiO_2 particles with an average diameter of 78 (±12) nm were obtained by adding APTES modified rhodamine B (RB-APTES) during synthesis resulting in ^{fx}S.

Table 1. XPS analysis of $P1_S$ and L-$P1_S$ immobilized on planar silica wafers.

Element	Atomic percentage [%]				
	Si wafer	$P1_S$ coatings		L-$P1_S$ coatings	
		pH 7.4	pH 4.0	pH 7.4	pH 4.0
O	35.7	29.7	30.4	30.5	29.7
C	9.3	51.2	50.6	42.5	40.0
Si	55.0	17.8	17.8	25.7	28.6
N	–	1.3	1.2	1.3	1.7
C/Si	0.2	2.9	2.9	1.7	1.0

In the next step, the as-synthesized SiO_2 particles were functionalized with the different polymers, using a silanization reaction between the triethoxysilane (TEOS) group of the linkers and the hydroxyl group of the silica surface, forming a covalent Si—O—Si bond. The coated SiO_2 particles are referred to as ^xS_P from now on where P indicates the polymer type (i.e., P1 for PHEMA, P2 for PCEA, and P3 for PEGMA). Janus (asymmetric) particles were made employing the Pickering emulsion method.[41] Specifically, $P3_{S/L}$ was deposited on the accessible hemisphere of the 80- and 500-nm SiO_2 particles in the Pickering emulsion, resulting in $^{80}JS_{P3S/L}$ and $^{500}JS_{P3S/L}$, respectively. Details on the individual motors' assembly are in Supporting Information Table S2, Supporting Information.

Bright-field microscopy images of the samples indicated that the high molecular weight polymers affected the stability of the colloids, resulting in aggregation for $^{500}S_{P1L}$ and $^{500}S_{P2L}$, which were therefore not further considered (Figure S2, Supporting Information). The polymer conjugation was confirmed by Fourier-transformed infrared (FTIR) spectroscopy (**Figure 3**). The spectrum of ^{500}S indicated the presence of Si—O bonds, with a strong vibrational band centered at 1065 cm^{-1} (black spectrum). New vibrational modes appeared (highlighted within the dotted rectangles) due to the polymer conjugation. The coating of $^{500}S_{P1S}$ was confirmed by the presence of the acrylate group (orange spectrum), displaying the characteristic C=O, C=C, and C—O—C stretching modes centered at 1650, 1460–1380, and 1090–1045 cm^{-1}, respectively. Further, the —CH_3 and —OH vibrational modes were observed in the regions of 2980–2880 and 3300 cm^{-1}, respectively. $^{500}S_{P2S}$ showed similar features due to the similar chemical structures of HEMA and

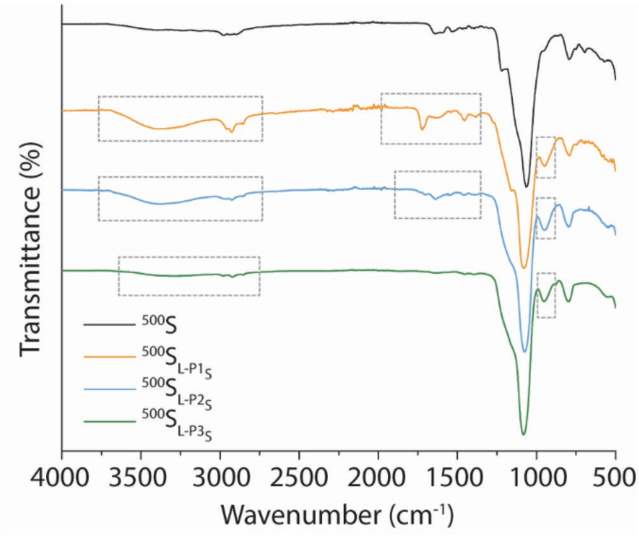

Figure 3. FTIR spectra of ^{500}S, $^{500}S_{L-P1S}$, $^{500}S_{L-P2S}$, and $^{500}S_{L-P3S}$. The grey rectangles denote the characteristic bands for the specific polymers.

CEA (blue spectrum). However, $^{500}S_{P3S}$ had only the vibrational bands characteristic of the $-CH_3$ and $-OH$ stretching modes as expected for PEGMA (green spectrum). Notice that the band centered at ≈1065 cm^{-1} changed from the wide band typical of the Si-O vibration to sharp peaks typical of the C−O−C vibration in all spectra.

Complementary, XPS analyses of the polymer coated particles were performed. For this purpose, the colloids were dried on a titanium-coated silica wafer to avoid the interference of the background signal from the silica wafer and the silica particles. The observed overall increase in the C/Si ratio in all the samples indicated that the polymer deposition was successful, while no C was detected for ^{500}S (Table S3, Supporting Information). Further, the N signal confirmed the polymer deposition, with the expected higher increase for polymer coatings containing L_2 due to their chemical structure.

2.5. Motion Experiments

With the aim to assess if polymer chain detachment from the particles' surface could result in enhanced mobility of the particles, the motors were exposed to a propagating pH gradient and their motion was recorded using an optical microscope. It was expected that the acidification of the environment caused the cleavage of the pH-labile linker, and the subsequent polymer coating disassembly resulted in a localized break in symmetry, allowing the particles to propel together with and in the direction of the acid front (**Figure 4**a).

First, the propagation of the pH front depending on the amount of added hydrochloric acid (HCl) to the inlet of the channel was assessed. The pH front propagation speed increased with increasing HCl concentration. The front propagation speeds were estimated from the derivatives of the position-time functions (Figure S3, Supporting Information), resulting in average values of 0.004, 0.045, and 0.063 μm s^{-1} for the concentrations of 0.1, 0.5, and 1.0 м HCl, respectively. The final pH in the channels after homogenization of the acid was found to be ≈4, ≈2, and ≈1 for 0.1, 0.5, and 1.0 м HCl, respectively.

Second, $^{500}S_{L\text{-}P1S}$, $^{500}S_{L\text{-}P2S}$, and $^{500}S_{L\text{-}P3S}$ were used as the pH-responsive motors, and $^{500}S_{P1S}$, $^{500}S_{P2S}$, and $^{500}S_{P3S}$ were chosen as the irresponsive controls. Specifically, the different assemblies were added into a bovine serum albumin (BSA)-coated microfluidic channel, and the locomotion was recorded for up to 1 min after adding different concentrations of HCl to the inlet of the channel (Figure 4a). When subjected to a pH gradient, the pH-responsive motors exhibited enhanced Brownian motion compared to the controls (Figure 4b(i)/c(i)/d(i)). This observation confirmed that the mobility was due to the polymer coating disintegration in the acidic environment and not due to the presence of the propagating pH front itself. A careful analysis of the trajectories indicated that most of the motors did not show directed locomotion, except for $^{500}S_{L\text{-}P2S}$ exposed to the steepest pH gradient. (Note: for these analyses, a new algorithm was employed, which only considers motors in the ensemble during their mobile phase. See Experimental Section for details). In addition, $^{500}S_{L\text{-}P3S}$ was the only motor that showed directed motion for the entire ensemble in all pH gradients. Further, $^{500}S_{L\text{-}P1S}$ and $^{500}S_{L\text{-}P2S}$ lost their mobility immediately after the acid front passed, while $^{500}S_{L\text{-}P3S}$ propelled for at least 1 min. These facts were also reflected in the MSD plots, where the diffusivities of $^{500}S_{L\text{-}P1S}$ and $^{500}S_{L\text{-}P2S}$ were similar to the controls exposed to the similar pH gradient (Figure 4b(ii)/c(ii) and Movies S1/S2, Supporting Information). Specifically, $^{500}S_{L\text{-}P1S}$ exhibited only enhanced Brownian motion and $^{500}S_{L\text{-}P2S}$ did change their random diffusion into weak ballistic motion, as illustrated by the change from linear to parabolic in the MSD plots. The diffusivity of $^{500}S_{L\text{-}P3S}$ increased substantially and indicated the turnover from simple random diffusion to proper ballistic motion, as evidenced both in the MSD plots, which became parabolic when the pH decreased (Figure 4d(ii)), and in the videos showing the motors' motion (Movie S3, Supporting Information).

Further, the whisker plots (for calculation details see the Motion Experiments section in Experimental Section 4) revealed that $^{500}S_{L\text{-}P1S}$ and $^{500}S_{L\text{-}P2S}$ had average and median velocities similar or even slower than the controls (< 0.5 μm s^{-1}) with an increasing part of the motors' population moving at very slow speeds (Figure 4b(iii)/c(iii)). Further, the mobility of $^{500}S_{L\text{-}P1S}$ and $^{500}S_{L\text{-}P2S}$ dropped after losing the polymer shell, indicated by the shorter trajectories or an even distribution of the motors' population ranging from traveling distances close to 0 up to ca. 10–12 μm (Figure 4b(iv)/c(iv)). We hypothesized that the change in the physicochemical properties of the polymers resulted in this lack of mobility. P1 tends to form hydrogels in solution, which might cause particle aggregation and hence, loss of locomotion. P2 becomes uncharged at acidic pH due to the protonation of the carboxyl groups, resulting in polymer collapse and eventual aggregation of the particles, also hindering their motion. Alternatively, P3 is both water-soluble and unaffected by pH changes; facts that might explain the enhanced locomotion when this polymer was employed.

The velocity of $^{500}S_{L\text{-}P3S}$ did not seem to be affected by the different pH, and only a slight increase from 0.5 to 1 μm s^{-1} was observed compared to the controls (Figure 4d(iii)). Nonetheless, the whisker plots did not show a large population of either very slow or non-mobile motors, illustrating that almost the entire motor population exhibited enhanced locomotion. The long trajectories of $^{500}S_{L\text{-}P3S}$ reached up to 20 μm traveling distance (Figure 4d(iv)).

In an effort to determine the effect of the polymer chain on the locomotion, $^{500}S_{L\text{-}P3L}$ was employed for comparison. These motors only showed a poor increase in mobility without a clear indication of ballistic motion. The whisker plots showed slow average velocities with a large part of the motors in the ensemble being very slow (Figure S4, Supporting Information). We speculate that this observation was probably related to the fact that the disassembly of the $P3_L$ brushes was either inefficient and/or resulted in an increased local viscosity that might have impaired the locomotion of these motors (Movie S4, Supporting Information).[42]

The final effort aimed to determine the mobility of the lead motor $^{500}S_{L\text{-}P3S}$ in cell media, since this is the relevant environment for any type of cell culture-based evaluation. The motors were dispersed in shallow, circular wells filled with cell media to mimic the actual environment when exposed to cells (**Figure 5**a and Movie S5, Supporting Information). As expected, the trajectories suggested no improved locomotion in comparison to

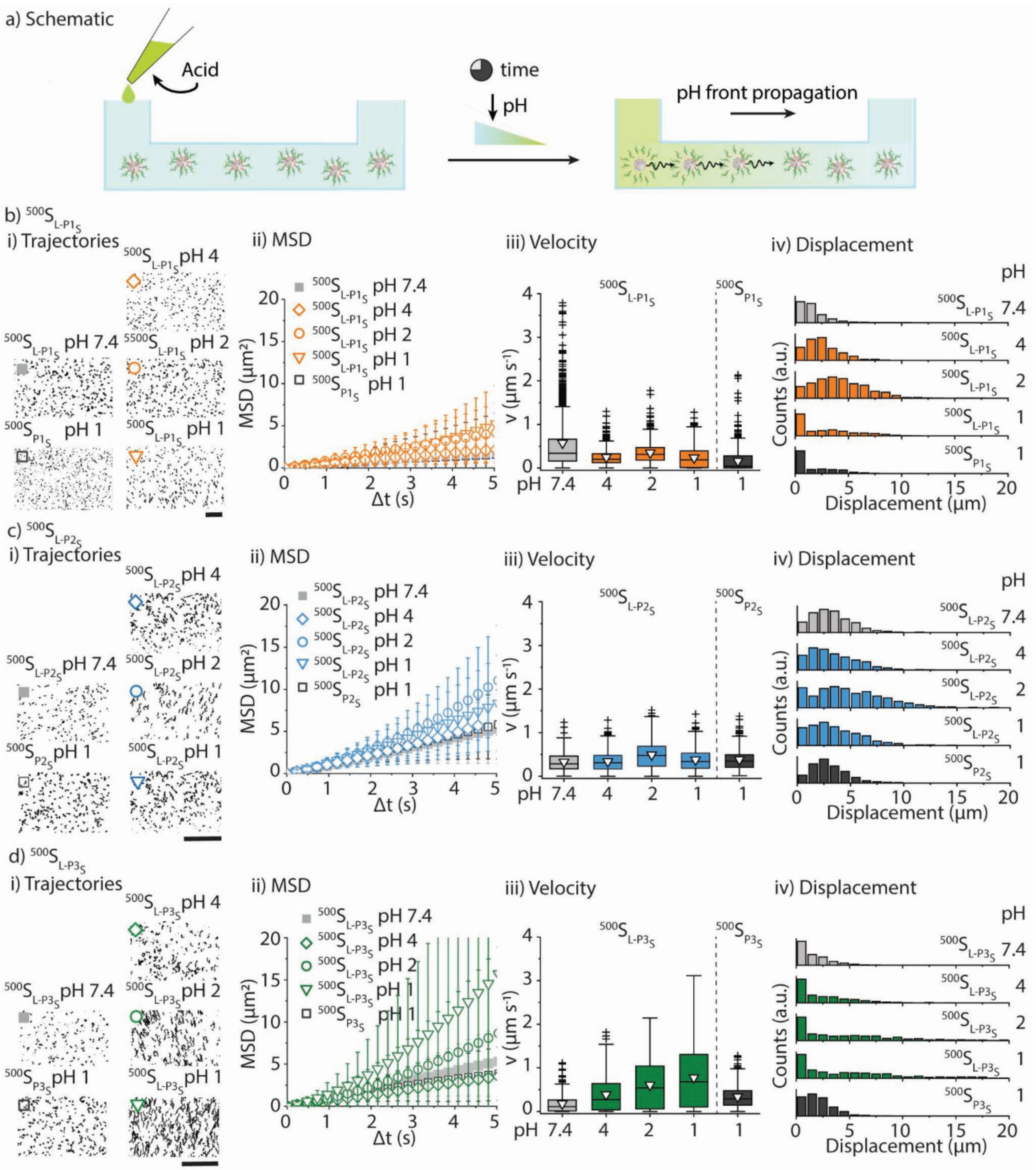

Figure 4. a) Cartoon illustrating the locomotion experiment. The acid front propagation triggers the polymer disassembly and the motor mobility. Locomotion properties in a pH gradient of b) $^{500}S_{L\text{-}P1S}$, c) $^{500}S_{L\text{-}P2S}$, and d) $^{500}S_{L\text{-}P3S}$. For every motor, the representative trajectories (i), MSD plots (ii), the velocities represented as whisker plots (iii), and the displacement (iv, zero excluded) are shown. Controls are shown in light grey and dark grey. For the MSD plots, data are presented as mean ± SD, n = 2. Scale bars are 100 µm.

the controls, since there was no break in symmetry for these homogenously coated motors that would result in propulsion, even upon polymer disassembly (Figure 5b(i), top panel). The MSD plots also corroborated this observation, showing no enhancement in diffusion or transition to ballistic motion (Figure 5b(ii), top panel). Further, the velocities of $^{500}S_{L\text{-}P3S}$ in

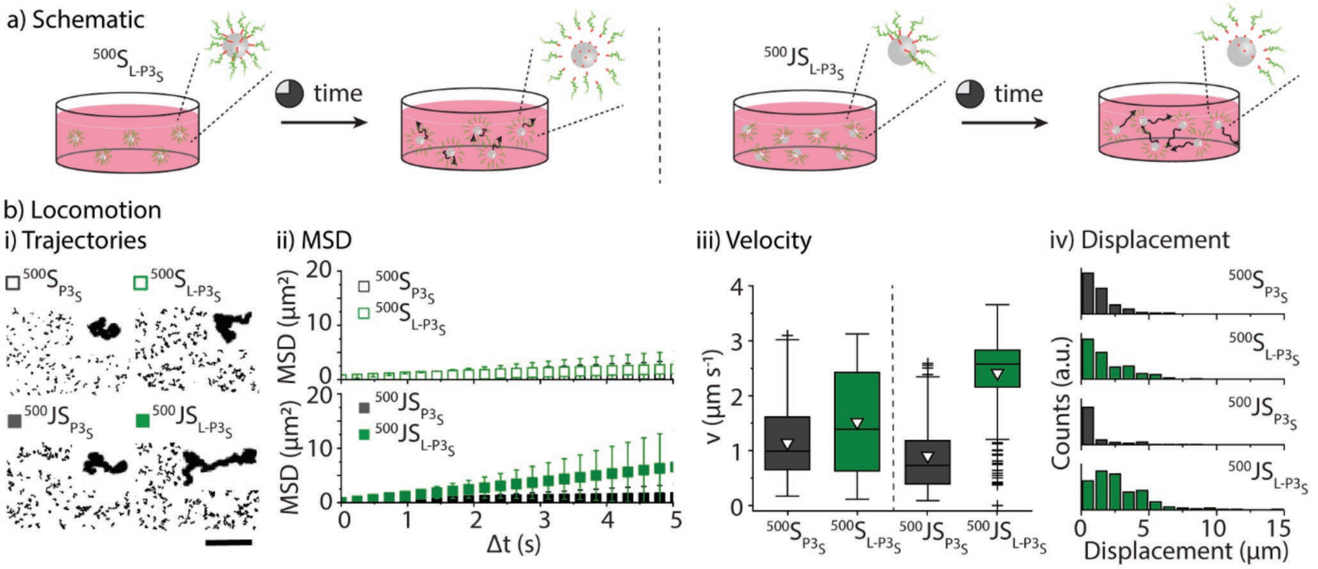

Figure 5. a) Cartoon illustrating the locomotion experiment in cell media. The pH-responsive linker is not stable over time and triggers the motor locomotion. b) Locomotion properties of ^{500}S$_{\text{L-P3S}}$ and ^{500}JS$_{\text{L-P3S}}$ in cell media. For every motor, the representative trajectories (i, insets: close-up of a single trajectory), MSD plots (ii), the velocities represented as whisker plots (iii), and the overall displacement (iv) are shown. Controls are shown in dark grey. For the MSD plots, data are presented as mean ± SD, n = 2. Scale bars are 100 µm.

cell media were comparable to ^{500}S$_{\text{L-P3S}}$ subjected to a propagating acid front (Figure 5b(iii), left). This was expected because of the crowded environment of the cell media, and the displacement of the motors was very short (i.e., <5 µm) (Figure 5b(iv), top panel).

In light of these results, we used Janus particles to improve the locomotion properties (i.e., ^{500}JS$_{\text{L-P3S}}$). Although the trajectories did not seem to improve at a first sight (Figure 5b(i), bottom panel), the MSD plots did reveal improved locomotion, as the slope became steeper (Figure 5b(ii), bottom panel). This was also shown in the whisker plots, where the population of ^{500}JS$_{\text{L-P3S}}$ showed a threefold increase in average velocity (Figure 5b(iii), right) compared to both the controls and the homogeneous motors. These motors displayed longer trajectories (up to 10–12 µm) (Figure 5b(iv), bottom panel), which suggested that they might result in good candidates for improved cellular uptake. It should be noted that the low stability of the acid-labile linker in cell media was not expected and cannot be explained in detail, but it cannot be attributed to an environmental pH change (Figure S5, Supporting Information).

2.6. Basic Biological Evaluation

Finally, the interaction of the motors with the murine macrophage-like cell line RAW 264.7 was studied. Macrophage-like cells are the type of cells that first interact with xenobiotics entering an organism. RAW 264.7 macrophages specifically are often used as a model for (nano)particle-screening to gain a basic understanding of the nanomaterial's cytotoxicity and intracellular fate.

Smaller-sized particles (80 nm) were chosen for the cell experiments to ensure that the uptake/association efficacy of the particles with the cells was not limited due to too large dimensions. The particles were core-labeled with rhodamine B to allow tracking by flow cytometry or confocal laser scanning microscopy (CLSM). As an initial biological evaluation, the short-term cytotoxicity of ^{f80}JS$_{\text{P3S}}$ and ^{f80}JS$_{\text{L-P3S}}$ was determined since the Janus particles were expected to interact with the RAW 264.7 macrophages to a higher degree than the homogenous particles (**Figure 6**a). A lactate dehydrogenase (LDH) assay was performed, indicating no influence on the cell membrane integrity after exposure of the cells to the particles for 24 h (Figure 6b). Then, uptake experiments were conducted in order to test the hypothesis of improved cellular uptake due to the observed increase in locomotion of ^{500}JS$_{\text{L-P3S}}$ compared to ^{500}JS$_{\text{P3S}}$ in cell media. To this end, ^{f80}JS$_{\text{P3S}}$ and ^{f80}JS$_{\text{L-P3S}}$ were mixed with cell media and incubated with RAW 264.7 macrophages for 1, 3, 6, and 24 h, followed by cell harvesting and analysis using flow cytometry (Figure 6c). The histograms of cells incubated with particles showed a broader distribution of fluorescence intensities compared to the cells-only controls, suggesting interaction of the cells with the motors. The association of the motors with the cells increased over time as indicated by the shift of the representative histograms towards higher fluorescent intensities (Figure 6c(i)). Histograms obtained from cells incubated with ^{f80}JS$_{\text{P3S}}$ only showed a slow gradual shift towards higher fluorescent intensities, while histograms from cells exposed to ^{f80}JS$_{\text{L-P3S}}$ exhibited a substantial shift towards higher fluorescence intensities already after 1 h. The slightly farther shift of histograms from cells exposed to ^{f80}JS$_{\text{L-P3S}}$ for 24 h compared to histograms of cells exposed to ^{f80}JS$_{\text{P3S}}$ was also reflected in the slightly increased normalized cell mean fluorescence (nCMF) (Figure 6c(ii)). There was a general trend observed that suggested an increased association of ^{f80}JS$_{\text{L-P3S}}$ with the cells compared to ^{f80}JS$_{\text{P3S}}$. However, there were no significant differences in the nCMF.

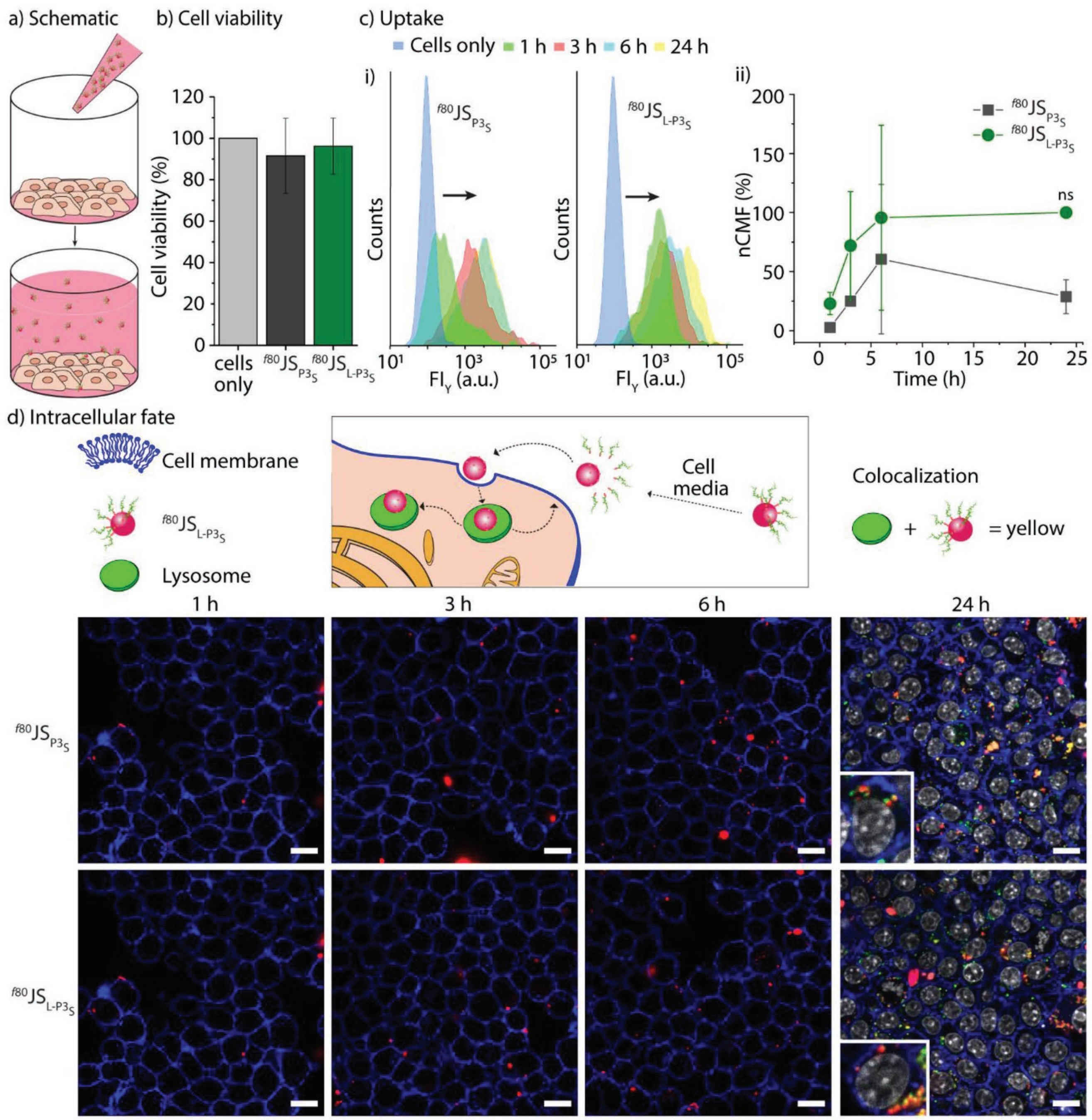

Figure 6. Interaction of $^{f80}\text{JS}_{\text{P3S}}$ and $^{f80}\text{JS}_{\text{L-P3S}}$ mixed in media with RAW 264.7 macrophages. a) Schematic illustrating the experimental set-up where the media mixed with the motors is added to the pre-seeded cells. b) Cell viability of RAW 264.7 macrophages incubated with $^{f80}\text{JS}_{\text{P3S}}$ or $^{f80}\text{JS}_{\text{L-P3S}}$ for 24 h, determined via LDH assay ($n = 3$). c) Representative histograms (i) and nCMF (ii) of the RAW 264.7 macrophages incubated with $^{f80}\text{JS}_{\text{P3S}}$ or $^{f80}\text{JS}_{\text{L-P3S}}$ for 1 h, 3 h, 6 h, or 24 h (F. I.: fluorescent intensity, $n = 3$). ns indicates no significant differences between $^{f80}\text{JS}_{\text{L-P3S}}$ and $^{f80}\text{JS}_{\text{P3S}}$ analyzed by one-way ANOVA using Šídák's post-hoc test. d) Representative CLSM images of the cells incubated with $^{f80}\text{JS}_{\text{P3S}}$ or $^{f80}\text{JS}_{\text{L-P3S}}$ for 1, 3, 6, or 24 h (red: $^{f80}\text{JS}_{\text{P3S}}$ or $^{f80}\text{JS}_{\text{L-P3S}}$; green: LysoTracker Green DND-26 stained lysosomes; blue: CellMask Deep Red Plasma Membrane Stain; white: Hoechst 33 342 stained nuclei) ($n = 2$–3). (All data are presented as mean ± SD). Scale bars are 10 µm.

Complementary, the cellular uptake of $^{f80}\text{S}_{\text{P3S}}$ and $^{f80}\text{S}_{\text{L-P3S}}$ was assessed after 1, 3, 6, and 24 h incubation, showing the expected neglectable uptake of these homogenously coated particles due to the known effect of PEG to minimalize interactions with biomolecules and cells (Figure S6a, Supporting Information).

Additionally, the uptake of the motors mixed with media and exposed to the cells was visualized using CLSM (Figure 6d).

Images were taken after 1, 3, 6, and 24 h exposure of the cells to ^{f80}JS$_{\text{P3S}}$ or ^{f80}JS$_{\text{L-P3S}}$ and staining of the cell membranes. An increase in uptake of both types of particles could be observed over time in agreement with the flow cytometry results. However, the images did not reveal any difference in interaction with the cells between ^{f80}JS$_{\text{P3S}}$ and ^{f80}JS$_{\text{L-P3S}}$. Additionally, the lower association of ^{f80}S$_{\text{P3S}}$ and ^{f80}S$_{\text{L-P3S}}$ with the cells was visually confirmed (Figure S6b, Supporting Information). In this case, larger aggregated clusters of particles were observed compared to the more evenly distributed fluorescent signal originating from ^{f80}JS$_{\text{P3S}}$ and ^{f80}JS$_{\text{L-P3S}}$. Further, ^{f80}JS$_{\text{P3S}}$ and ^{f80}JS$_{\text{L-P3S}}$ were localized with the lysosomes after 24 h incubation time (Figure 6d, far-right column and Figure S6c(i)/(ii), Supporting Information, for split channels), that is, the yellow color resulting from the overlap of stain for the lysosomes (LysoTracker in green) and the particles (in red) indicated entrapment of the latter in the lysosomes. As a semi-quantitative method to assess the escape efficacy, the Manders' correlation coefficient (MCC) was calculated. An MCC of 0.93 ± 0.03 was obtained for both types of particles when considering the fraction of ^{f80}JS$_{\text{P3S}}$ or ^{f80}JS$_{\text{L-P3S}}$ correlated with the lysosomes, indicating that the vast majority of particles were colocalized with the lysosomes. On the other hand, when the fraction of lysosomes correlated with ^{f80}JS$_{\text{P3S}}$ and ^{f80}JS$_{\text{L-P3S}}$ was considered, an MCC of 0.72 ± 0.02 and 0.77 ± 0.08 was obtained for ^{f80}JS$_{\text{P3S}}$ and ^{f80}JS$_{\text{L-P3S}}$, respectively. These slightly lower MCC values in the latter case reflected that not all lysosomes contained particles but also that lysosomes, which were not involved in the uptake of particles, were stained. Consequently, the pH-sensitive linker did not facilitate lysosomal escape in RAW 264.7 macrophages, likely due to its premature disintegration in cell media prior to endocytosis.

With the goal to determine if the enhanced mobility of the motors in cell media could be beneficial for their ability to approach and interact with cells, we deposited 10 µL of the motors on top of the media of a cell-containing well instead of premixing the media with the motors before exposure to the cells (**Figure** 7a(i)). The representative histograms of cells exposed to ^{f80}JS$_{\text{P3S}}$ showed that it took up to 6 h for these histograms to shift towards higher fluorescent intensities due to the association of the motors with the cells (Figure 7a(ii)). In contrast, histograms obtained for cells exposed to ^{f80}JS$_{\text{L-P3S}}$ started to shift towards higher cell fluorescent intensities already after 1 h. Consequently, significantly higher nCMF values were found for cells incubated with ^{f80}JS$_{\text{L-P3S}}$ for 6 or 24 h compared to cells exposed to ^{f80}JS$_{\text{P3S}}$ (Figure 7a(iii)). Last, the aim was to ensure that the difference in nCMF could not be attributed to the fact that ^{f80}JS$_{\text{P3S}}$ was half-coated with PEG, a polymer that hinders uptake of nanoparticles by cells, while ^{f80}JS$_{\text{L-P3S}}$ lost its PEG chains. To this end, ^{f80}JS$_{\text{L-P3S}}$ were suspended in cell media overnight to allow for the removal of the polymer chains (refer to as ^{f80}JS$_{\text{L-P3S after media}}$). These particles were washed and resuspended in water and locally added on top of the media of a cell-containing well and let to incubate for 24 h (Figure 7b(i)). The nCMF of cells exposed to ^{f80}JS$_{\text{L-P3S after media}}$ only showed ≈50% of the nCMF of cells treated with ^{f80}JS$_{\text{L-P3S}}$, and no significant differences to the nCMF of cells exposed to ^{f80}JS$_{\text{P3S}}$ (Figure 7b(ii)). This latter finding suggested that enhanced locomotion was the major contributing factor that allowed for more efficient association of ^{f80}JS$_{\text{L-P3S}}$ to the cells.

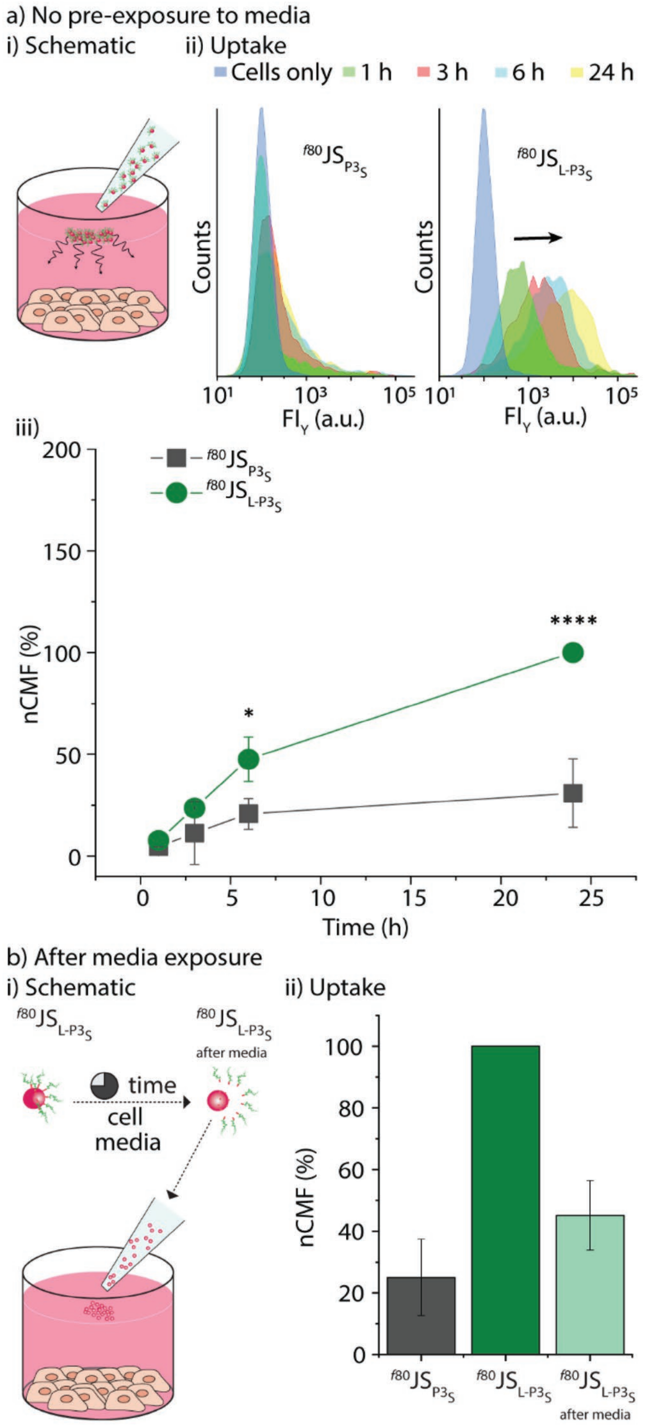

Figure 7. Interaction of locally deposited ^{f80}JS$_{\text{P3S}}$ and ^{f80}JS$_{\text{L-P3S}}$ with RAW 264.7 macrophages. a) Schematic illustrating the local deposition of ^{f80}JS$_{\text{P3S}}$ and ^{f80}JS$_{\text{L-P3S}}$ in the well with pre-seeded i) RAW 264.7 macrophages, ii) representative histograms, and iii) nCMF of the RAW 264.7 macrophages incubated with ^{f80}JS$_{\text{L-P3S}}$ or ^{f80}JS$_{\text{P3S}}$ for 1, 3, 6, or 24 h ($n = 3$). *$p < 0.05$, and ****$p < 0.0001$ indicate significant differences between ^{f80}JS$_{\text{L-P3S}}$ and ^{f80}JS$_{\text{P3S}}$ analyzed by one-way ANOVA using Šídák's post-hoc test. b) i) Schematic illustrating the pre-exposure of ^{f80}JS$_{\text{L-P3S}}$ to media and the local deposition of ^{f80}JS$_{\text{L-P3S after media}}$ in the well with pre-seeded RAW 264.7 macrophages. ii) nCMF of the RAW 264.7 macrophages incubated with ^{f80}JS$_{\text{P3S}}$, ^{f80}JS$_{\text{L-P3S}}$, or ^{f80}JS$_{\text{L-P3S after media}}$ for 24 h ($n = 2$–3). Data are presented as mean ± SD.

3. Conclusion

We illustrated that the pH-triggered detachment of polymers from motor surfaces could be used to initiate locomotion in motors resulting in ballistic motion with top speeds of 1–3 µm s^{-1}. The low stability of the pH-labile linker in cell media was utilized to reduce the time required for cells to internalize the motors. However, due to the premature loss of the polymer coating, these motors remained trapped in the lysosomes.

Future efforts towards enhanced lysosomal escape of polymer-based motors using their thrust to enter the cytosol will consider the use of pH-labile linkers that will be stable in cell media or linkers that will selectively respond to lysosomal enzymes.

4. Experimental Section

Materials: Tetraethylorthosilicate (TEOS), hexadecyltrimethylammonium bromide (CTAB), ammonium hydroxide (NH_4OH 29 wt.%), 2-hydroxyethyl methacrylate (HEMA), 2-carboxyethyl acrylate (CEA), poly(ethylene glycol) methyl ether methacrylate (PEGMA, average Mn 500), rhodamine B, sodium ascorbate, copper(II) sulfate ($CuSO_4$), tris[2-(dimethylamino)ethyl]amine (Me_6TREN), (3-aminopropyl)triethoxysilane (APTES), N-(3-dimethylaminopropyl)-N′-ethylcarbodiimide hydrochloride (EDCl), N-hydroxysuccinimide (NHS), α-bromoisobutyryl bromide, and bovine serum albumin (BSA), phosphate-buffered saline (PBS), bisbenzimide H 33 342 trihydrochloride (Hoechst 33 342), and Dulbecco's Modified Eagle's Medium were purchased from Sigma-Aldrich. 4-Dimethylaminopyridine (DMAP), triethyl amine (TEA), 4-hydroxybenzaldehyde, 1,4-phenylenediamine, di-*tert*-butyl decarbonate, trifluoroacetic acid (TFA), 4-carboxybenzaldehyde, and N,N'-dicyclohexylcarbodiimide (DCC) were purchased from Acros Organics. Hydrogen peroxide (H_2O_2) and paraffin wax were commercially available from Merck KGaA (Germany). Sulfuric acid (H_2SO_4), anhydrous sodium sulfate (Na_2SO_4), sodium hydrogen carbonate (Na_2HCO_3), ethanol, dichloromethane (DCM), dimethyl sulfoxide (DMSO), ethyl acetate, n-hexane, chloroform, hydrochloric acid (37%, HCl), and tetrahydrofuran (THF) were purchased from VWR. µ-Slides VI 0.4 uncoated were purchased from ibidi GmbH. CyQUANT LDH Cytotoxicity Assay and CellMask Deep Red plasma membrane stain were obtained from Thermo Fisher Scientific. Fetal bovine serum (FBS) and LysoTracker Green DND-26 were purchased from Invitrogen, and penicillin–streptomycin (10 000 U mL^{-1}) was purchased from Gibco. Ultrapure water (18.2 MΩ cm resistance) was provided by an ELGA Purelab Ultra system.

HEPES buffer (10 mM HEPES and 50 mM NaCl in ultrapure water, pH 7.4) and Na_2HPO_4 buffer (2.5 mM Na_2HPO_4 and 50 mM NaCl in ultrapure water, pH 4.0) were employed to control the pH throughout the experiments.

Non-Labeled Silica (SiO_2) Particle Synthesis: Silica (SiO_2) particles of ca. 80 and 500 nm were prepared following a modified Stöber method.[43] For the 80 nm particles, 10.8 mL ultrapure water, 80.6 mL ethanol, and 2.36 mL NH_4OH (28 wt.%) were mixed in a flask and sonicated for 10 min. Next, 6.24 mL TEOS was added to the solution and sonicated for 10 min. The resulting cloudy solution was left to stand overnight and finally centrifuged to remove the supernatant. The thus obtained silica particles were washed repeatedly with water and ethanol (5000 rpm, 10 min), and finally kept in water and stored in a fridge. For the 500 nm particles, 325 mg of CTAB were dissolved in a mixture of 50 mL ethanol and 125 mL ultrapure water and stirred until complete dissolution. Next, 1.5 mL of NH_4OH (29 wt.%) were added under stirring, and finally 2 mL of TEOS (50 vol. % in ethanol) were added dropwise. The solution was allowed to react overnight at room temperature. Finally, the particles were washed with ethanol (5000 rpm, 10 min, 3×) and stored in ethanol until further use.

Fluorescently-Labeled SiO_2 Particles Synthesis: For the cell experiments, fluorescently labeled SiO_2 particles were made by adding APTES-modified rhodamine B (RB-APTES) during the particle synthesis.

RB-APTES was made by dissolving rhodamine B (2 mmol, 0.96 g), EDCl (4 mmol, 0.77 g), and DMAP (4 mmol, 0.49 g) in DCM (40 mL). The solution was stirred at room temperature for 1 h. Then APTES (3 mmol, 0.66 g) was dissolved in DCM (10 mL) and added dropwise to the solution. The reaction was stirred at room temperature overnight. After that, the solvent was evaporated and the crude product was purified with column chromatography using hexane: ethyl acetate (3:1, v/v) as the eluent, which gave the pure product RB-APTES as a slightly pink oil.

Then, the particles were made by mixing 10.8 mL ultrapure water, 80.6 mL ethanol, and 2.36 mL NH_4OH (28 wt.%) in a flask followed by sonication for 10 min. 6.24 mL TEOS and RB-APTES (0.58 g, 10 wt.% of TEOS) were added to the solution and sonicated for 10 min. The resulting cloudy solution was left to stand overnight and finally centrifuged to remove the supernatant. The thus obtained pink silica particles were washed repeatedly with water and ethanol (5000 rpm, 10 min), and stored in water in a fridge.

All particles were visualized using transmission electron microscopy (TEM). TEM images were taken with a Tecnai G2 Spirit Instrument, working at an acceleration voltage of 100 kV. Samples for TEM were deposited in copper/Formvar/carbon grids (300 mesh) and allowed to dry. The particle size was determined by averaging the diameter of ≈200 particles from TEM images using the Fiji software. The Gaussian function was utilized for the size distribution analysis, indicated as $\bar{x} \pm 2s$ (average plus/minus 2× std. dev., for 95.4% of the population).

Synthesis of Linker L_0: APTES (12 mmol, 2.6 g) and TEA (30 mmol, 3.0 g) were dissolved in anhydrous DCM (30 mL). The solution was cooled down in an ice bath. α-Bromoisobutyryl bromide (10 mmol, 2.3 g) was dissolved in anhydrous DCM (10 mL) and added dropwise to the solution. The mixture was stirred at room temperature overnight. After that, the solvent evaporated and the crude product was purified with column chromatography using hexane : DCM = (3:1, v/v) as the eluent, which gave the product as a colorless oil.

Synthesis of Linker L_1: 4-Hydroxybenzaldehyde (32.8 mmol, 4 g) and TEA (98.4 mmol, 9.95 g) were dissolved in anhydrous THF (100 mL) and cooled down in an ice bath. α-bromoisobutyryl bromide (39.3 mmol, 9.04 g) was added dropwise to the solution. The reaction was left to stir overnight at room temperature. Then, the solvent was evaporated and ethyl acetate (100 mL) was added to dissolve the residue followed by 2× washing with brine. The organic phase was collected and dried over anhydrous Na_2SO_4. The pure product was obtained after purification with column chromatography using hexane : DCM = 1:1 (v/v) as the eluent.

The product from the last step (1.35 g, 5 mmol) and TEA (1.52 g, 15 mmol) were dissolved in anhydrous DCM (30 mL) and cooled down in an ice bath. To the solution, APTES (1.33 g, 6 mmol) in anhydrous DCM (5 mL) was added dropwise. The reaction was left to continue overnight. After that, the solvent was evaporated and the crude product was purified with column chromatography using hexane : DCM = 1:2 (v/v) as the eluent, which gave the product as a yellowish solid.

Synthesis of Linker L_2: 1,4-Phenylenediamine (50 mmol, 5.4 g) was suspended in DCM (200 mL). To the solution, di-*tert*-butyl decarbonate (20 mmol, 4,37 g) was added in one portion, followed by a catalytic amount of DMAP (2.5 mmol, 305 mg). The mixture was stirred at room temperature for 24 h. After that, the crude product was purified with column chromatography using ethyl acetate : hexane = 2:1 (v/v) as the eluent, which gave the product as a slightly yellowish solid.

The product from the last step (3.74 mmol, 0.77 g) and TEA (11.2 mmol, 1.13 g) were dissolved in anhydrous DCM (30 mL). The solution was cooled down in an ice bath. To the solution, α-bromoisobutyryl bromide (1.5 mmol, 1.29 g) in anhydrous DCM (10 mL) was added dropwise. Afterwards, the reaction was left to react overnight at room temperature. The crude product was purified with column chromatography using hexane : ethyl acetate (2:1) as the eluent, which gave the pure product as a yellowish solid.

The product from the last step (1.23 mmol, 440 mg) was dissolved in a mixture of DCM (15 mL) and TFA (15 mL) in an ice bath. Then the reaction was continued at room temperature overnight and confirmed the full consumption of the starting material with TLC. The flask was cooled down in an ice bath again and a saturated solution of $NaHCO_3$ was added slowly to neutralize the excess TFA. The organic phase was washed with water 3× and dried over anhydrous Na_2SO_4. After evaporation, the pure product was obtained as a gray solid, which was used in the next step without extra purification.

4-Carboxybenzaldehyde (10 mmol, 1.5 g) was suspended in THF (40 mL). To this solution, NHS (15 mmol, 1.73 g) and DCC (15 mmol, 3.09 g) were added in one portion. The mixture was stirred at room temperature for 4 h. The precipitate was filtered off and the filtrate was concentrated. The crude product was purified with column chromatography using hexane : DCM = 1 : 5 (v/v) as the eluent, which gave the product as a white solid.

The product from the last step (1.62 mmol, 400 mg) and TEA (4.86 mmol, 490 mg) were dissolved in DCM (30 mL) and cooled down in an ice bath. To the solution, APTES (2.1 mmol, 465 mg) in anhydrous DCM (10 mL) was added dropwise. The reaction was left to continue overnight at room temperature. After that, the solvent was evaporated and the crude product was purified with column chromatography using hexane: ethyl acetate (1:1, v/v) as the eluent, which gave the pure product as a colorless viscous oil.

The amine (0.226 mmol, 58 mg) was dissolved in anhydrous ethanol (2 mL). The aldehyde (0.226 mmol, 80 mg) was dissolved in anhydrous ethanol (1 mL) and added dropwise to the solution. The mixture was refluxed overnight and cooled down to room temperature. After that, the solvent was evaporated and a minimum amount of DCM was added to dissolve the crude product. To the solution, diethyl ether (40 mL) was added to induce precipitation. The precipitate was filtered and washed repeatedly with diethyl ether, which gave the product L_2 as a pale yellow solid.

Stability of the Linkers: The stability of L_1 and L_2 was assessed by monitoring the time-dependent absorption of both linkers at pH between 2 and 7.4. For that, L_1 or L_2 (50 µg mL^{-1}) were dissolved in the corresponding buffer and a multimode plate reader (Perkin Elmer) was used to record the absorbance at $\lambda = 373$ nm for L_1 and 350 nm for $\lambda = L_2$ every 5 min for 1 h. The stability of L_2 in cell media was monitored over 6 h instead.

Poly(2-Hydroxyethyl Methacrylate) (P1) Synthesis: L_0 or L_2 (0.1 mmol), 2-hydroxyethyl methacrylate (5 mmol, 650 mg), and tris[2-(dimethylamino)ethyl]amine (67 µL, 0. 25 mmol) were dissolved in anhydrous DMSO (2 mL). The mixture was protected under N_2 atmosphere. CuCl (0.12 mmol, 12 mg) was suspended in anhydrous DMSO (0.5 mL) and bubbled with N_2 for 10 min. After that, the CuCl solution was transferred and the two mixtures were combined. The solution was reacted for 1 or 24 h at room temperature. Afterward, the reaction mixture was added dropwise to a large volume of DCM (50 mL) to induce precipitation. The precipitates were collected by centrifugation and washed 3× with DCM, which gave the polymer PHEMA as a white solid.

Poly(2-Carboxyethyl) Acrylate (P2) Synthesis: P2 was synthesized in the same manner as P1 except that 2-carboxyethyl acrylate was used as the monomer instead of 2-hydroxyethyl methacrylate and the reaction time was 1 or 24 h.

Poly(Ethylene Glycol) Methyl Ether Methacrylate (P3) Synthesis: P3 was synthesized in the same manner as P1 except that poly(ethylene glycol) methyl ether methacrylate (average M_n 500) was used as the monomer instead of 2-hydroxyethyl methacrylate and the reaction time was 1 or 5 h.

Planar Surfaces: The deposition and disruption of L-P1$_S$, L-P1$_L$, P1$_S$, and P1$_L$ were assessed by X-ray photoelectron spectroscopy (XPS). Silicon wafers were cut into 10 × 10 mm^2 squares and cleaned with freshly prepared piranha solution (H_2O_2:H_2SO_4 in a 3:7 vol. ratio) for 30 min. (Caution: piranha solution was highly reactive and great care must be taken when handling it.) The crystals were rinsed with ultrapure water and then thoroughly washed with ethanol and ultrapure water followed by drying under an N_2 flow. Then, the silicon crystals were functionalized with the different polymers. For that, the crystals were placed in a 5-mL glass vial and either L-P1$_S$ or L-P1$_L$ (1 mg mL^{-1}) was added and left to react overnight at room temperature. Next, the crystals were again washed with ethanol and ultrapure water followed by drying under an N_2 flow. Afterwards, the crystals containing the polymer were exposed to pH 7.4 or pH 4.0 for 2 h, followed by washing with ethanol and ultrapure water and dried under an N_2 flow. Clean silicon crystals and P1$_S$ or P1$_L$ functionalized crystals exposed to pH 7.4 and pH 4.0 were used as controls. The XPS experiment was carried out using a monochromated Al Kα X-ray source (1486.7 eV) operated at 150 W and residual pressure in the 10^{-9} torr range on a Kratos Axis UltraDLD spectrometer. Survey scans were collected with 160 eV analyzer pass energy and 1.0 eV step size. CasaXPS software–version 2.3.16 (Casa Software Ltd, Wilmslow, Cheshire, UK) was used to process the spectra. The spectra were calibrated by setting the Si2p peak to 99.0 eV. The atomic surface concentrations represent the average of survey scans taken at three different spots on each sample, and two independent repeats were exercised.

Polymer Deposition: L-P1$_{S/L}$, L-P2$_{S/L}$, L-P3$_{S/L}$, P1$_{S/L}$, P2$_{S/L}$, and P3$_{S/L}$ (6 mg) were dissolved in methanol (950 µL) and added to silica particles (30 mg). Deionized water (50 µL) was added, and the mixture was reacted at room temperature for 3 days. Afterward, the silica particles were collected by centrifugation and washed 3× with methanol, ethanol, and finally dispersed in ethanol to prevent the hydrolysis of the imine. Prior to use, the ethanol solution was replaced with water by centrifugation. The yielded particles were referred to as ^{x}S$_P$, where x is the particle diameter (nm) and P is the type of immobilized polymer.

Fourier transformed infrared spectroscopy (FTIR) was employed, using a Perkin Elmer Spectrum Two spectrophotometer with a $LiTaO_3$ detector working in ATR (attenuated total reflectance) mode was used to assess the polymer immobilization. ^{500}S$_P$ were washed (6000 rpm, 2 min) and redispersed in ethanol to assess the FITR measurement. 10 µL of each sample were deposited onto the diamond crystal and allowed to dry. 4 scans were recorded between 450–4000 cm^{-1} with a resolution of 1 cm^{-1}.

XPS was also exercised on the colloids to determine the polymer deposition. For that, silicon wafers were cut into 10 × 10 mm^2 squares and a titanium layer was deposited on the surface to avoid interferences from the silica originating from the substrate. Then, the crystals were cleaned with freshly prepared piranha solution (H_2O_2:H_2SO_4 in a 3:7 vol. ratio) for 30 min. The crystals were rinsed with ultrapure water and then thoroughly washed with ethanol and ultrapure water followed by drying under an N_2 flow. Then, the crystals were functionalized with the different colloids. ^{500}S$_{\text{L-P1S}}$, ^{500}S$_{\text{L-P2S}}$, ^{500}S$_{\text{L-P3S}}$, and ^{500}S$_{\text{L-P3L}}$ were deposited on the crystals and left to react for 2 h. Next, the crystals were again washed with ethanol and ultrapure water followed by drying under an N_2 flow. Clean titanium-modified crystals and ^{500}S functionalized crystals were used as controls. The XPS experiment was conducted as outlined before.

Motion Experiments: BSA-coated microfluidic channels were used to assess the locomotion. For that, the channels were filled with a solution of BSA (1 mg mL^{-1}) and allowed to functionalize for 1 h. Next, the channels were rinsed with HEPES buffer (pH 7.4) before use.

^{500}S$_{\text{L-P1S}}$, ^{500}S$_{\text{L-P2S}}$, and ^{500}S$_{\text{L-P3S}}$ were diluted 10× in HEPES buffer (pH 7.4), vortexed and then transferred into a µ-Slides VI 0.4 microfluidic channel (Ibidi GmbH) coated with BSA. ^{500}S$_{\text{P1S}}$, ^{500}S$_{\text{P2S}}$, and ^{500}S$_{\text{P3S}}$ were considered as controls. The samples were added to the microfluidic channel and left to stabilize for 5 min. Next, 5 µL of HCl (0, 0.1, 0.5 or 1.0 M, final pH 7.4, 4, 2, and 1, respectively) were added to the channel, and the movies were collected right after for 1.5 min using a bright-field microscopy (Olympus IX81) at 16.67 fps using a 60× oil objective. For the Janus motors ^{500}JS$_{\text{L-P3S}}$, Ibidi treat µ-Slides 18 well-flat/low volume were used (Ibidi GmbH). The trajectories of individual motors were tracked by using the Fiji plugin "TrackMate".[44] The trajectories were then extracted and imported to Matlab, in which the mean-squared displacement (MSD) analysis was exercised, using a protocol published elsewhere.[45] The locomotion performance of the motors was analyzed according to the following equation $\mathrm{MSD} = 4D_{\mathrm{eff}}\Delta t + \nu^2\Delta t^2$, where D_{eff} and ν stand for the effective diffusion coefficient and the average velocity, respectively. For motors undergoing only Brownian (random) motion, the quadratic term of the equation approximates to zero, whereas for those displaying directed (ballistic) motion, D_{eff} becomes negligible. The error bar given in the plots was the standard deviation of the mean. Note that the larger error bars at longer times in the MSD plots were a result of the cumulative errors for every time shift. Whisker plots of the median velocity of all motors were exercised using the in-house developed Python scripts which are available as Supporting Information section (zip folder "swim-trackcode_SI" with sample data measured from optical tracking experiments analyzed in Figure 4). This folder also contains all analysis scripts used to produce the whisker plots and histograms, written in Python programming language. The added README file contains instructions for use. The whisker plots (or boxplots) present the average velocity (line crossing each box), the median (triangle), and the first and third quartiles (lower and upper edges of the box). Outliers are indicated as crosses. To obtain the velocity whisker plots, first, each recorded motor trajectory was discretized into time intervals $\Delta\tau_i$ equal to the duration of the camera frame, that is, $\Delta\tau_i = 1/16.67$ s. Then the corresponding "instantaneous" motor displacements $r_{\Delta\tau_i}$ during $\Delta\tau_i$ were calculated as $r_{\Delta\tau_i} = \sqrt{x^2_{\Delta\tau_i} + y^2_{\Delta\tau_i}}$, with $x_{\Delta\tau_i}$ and $y_{\Delta\tau_i}$ being the planar coordinate changes recorded by the tracking camera during the time instants Δt_i. In the next step, the average velocity ν was calculated for each motor trajectory by summing only the instantaneous contributions with non-zero displacement, that is, $\nu = R/T$, where the total length $R = \sum_i r_{\Delta\tau_i}$ and the total time duration $T = \sum_i \Delta\tau_i$ were evaluated by summing only those trajectory contributions with $r_{\Delta\tau_i} > 0$. This method allowed the exclusion of the static motor trajectory contributions $\Delta\tau_i$ which would otherwise lead to underestimated velocities.

Cell Experiments: Macrophage-like murine RAW 264.7 cells were obtained from the European Collection of Authenticated Cell Cultures and cultured in 25 cm^2 culture flasks at 37 °C and 5% CO_2. Dulbecco's Modified Eagle's Medium was used containing 4500 mg L^{-1} glucose, sodium bicarbonate, and sodium pyruvate (passage window of the cells: 12–25). The medium was supplemented with 10% FBS and 1% streptomycin/penicillin.

Cell Viability: RAW 264.7 macrophages were seeded in 96-well plates with a concentration of 30 000 cells per well. The plates were incubated at 37 °C and 5% CO_2 overnight. $^{f80}\mathrm{JS}_{\mathrm{L\text{-}P3S}}$ or $^{f80}\mathrm{JS}_{\mathrm{P3S}}$ (≈4.3 µg per well) were resuspended in media (including FBS) and added to the wells not exceeding 10 vol% in 100 µL of media. The concentration of the stock solutions of the particles was adjusted according to the fluorescence intensity obtained from plate reader measurements to ensure exposure of the cells to similar amounts of particles. Wells with cells not exposed to particles served as controls and all samples were incubated for 24 h at 37 °C and 5% CO_2. The LDH assay was performed by transferring 50 µL of media from each well to a new black 96-well plate and adding 50 µL of reagent mixture to each of the wells followed by incubation at room temperature for 10 min. Then, 50 µL of stop solution was added, and the fluorescent intensity ($\lambda_{\mathrm{ex/em}} = 560/590$ nm) was measured using a multimode plate reader. Spontaneous LDH was reflected by the signal of non-treated cells, whereas maximum LDH corresponded to the signal of lysed cells. The cells were lysed by the addition of 10 µL of 10× lysis buffer and incubation at 37 °C and 5% CO_2 for 45 min prior to the addition of reagent mix and stop solution. Three independent repeats for each sample were conducted. The background fluorescence of only media was subtracted from all values and the cell viability was calculated as follows:

$$\text{Cell viability}\,(\%) = 100\% - \left(\frac{\text{compound treated LDH} - \text{spontaneous LDH}}{\text{maximum LDH} - \text{spontaneous LDH}} \times 100\right) \tag{1}$$

Cellular Uptake: The uptake of the motors by RAW 264.7 macrophages was evaluated by flow cytometry. Cells were seeded in 96-well plates with a concentration of 50 000 cells per well and incubated at 37 °C and 5% CO_2 overnight. Next, $^{f80}\mathrm{JS}_{\mathrm{L\text{-}P3S}}$, $^{f80}\mathrm{JS}_{\mathrm{P3S}}$, $^{f80}\mathrm{S}_{\mathrm{L\text{-}P3S}}$, or $^{f80}\mathrm{S}_{\mathrm{P3S}}$ (≈4.3 µg per well) were added to the cells by two different methods: either premixed in 100 µL of media or suspended in water and carefully added dropwise into the fresh media covering the cells (10 v%) without further agitation. To obtain particles pre-exposed to media, $^{f80}\mathrm{JS}_{\mathrm{L\text{-}P3S}}$ were suspended in cell media and let stand overnight, spun down, and resuspended in water. The plates were incubated for 1, 3, 6, and 24 h at 37 °C and 5% CO_2. Following, the cells were washed twice with cell media, detached from the wells by scraping, and suspended in 200 µL of cell media. The cell mean fluorescence (CMF) was analyzed using a flow cytometer ($\lambda_{\mathrm{ex}} = 488$ nm) (Guava easyCyte Single Sample Flow Cytometer, Merck). The autofluorescence of untreated cells was subtracted and the values were normalized by the CMF of $^{f80}\mathrm{JS}_{\mathrm{L\text{-}P3S}}$ or $^{f80}\mathrm{S}_{\mathrm{L\text{-}P3S}}$.

Intracellular Fate: The uptake of the particles by the cells was visualized using CLSM. To this end, RAW 264.7 macrophages (300 000 cells in 1 mL cell media) were seeded in a cell culture imaging dish (35 mm confocal dish, VWR) and allowed to adhere overnight at 37 °C and 5% CO_2. $^{f80}\mathrm{JS}_{\mathrm{L\text{-}P3S}}$ or $^{f80}\mathrm{JS}_{\mathrm{P3S}}$ (≈13 µg resuspended in 1 mL media) were added to each confocal dish and left to incubate for 1, 3, 6, and 24 h at 37 °C and 5% CO2. Furthermore, $^{f80}\mathrm{S}_{\mathrm{P3S}}$ or $^{f80}\mathrm{S}_{\mathrm{L\text{-}P3S}}$ were added to the cells to incubate for 1 h and 24 h. The cells were washed twice with PBS and the samples after 24 h incubation with $^{f80}\mathrm{JS}_{\mathrm{P3S}}$ or $^{f80}\mathrm{JS}_{\mathrm{L\text{-}P3S}}$ were stained with LysoTracker. Here, LysoTracker Green DND-26 was diluted in prewarmed media to a final concentration of 100 nM. The area containing the cells was covered with 120 µL of the lysotracker-containing media, followed by 45 min of incubation at 37 °C and 5% CO_2 and washing twice with PBS. Nuclei were stained with Hoechst 33 342 by incubating the cells with a 1:200 dilution in PBS for 15 min at room temperature. All samples were incubated with CellMask Deep Red Plasma membrane stain (5 µg mL^{-1} in 120 µL of cell media) for 5 min. PBS (1 mL) was added for storage after washing twice. The cells were visualized using a Zeiss LSM700 CLSM. Five images at random locations with the same settings were taken per sample, and three independent experiments with CellMask stain or two independent experiments with additional LysoTracker staining were performed. The gain of the images has been artificially enhanced afterward for better visualization without any influence on the colocalization calculations. The colocalization of the particles with the lysosomes was determined via the Manders' colocalization coefficient (MCC) using the Coloc 2 plug-in for ImageJ after subtraction of the background (50 pixel ball pen size) for all images.

Statistical Analysis: Statistical significance was determined by one-way ANOVA followed by Šídák's multiple comparison test using GraphPad Prism version 9. 0. 0 for Windows. A $p < 0.05$ was considered statistically significant and it is presented as follows, $*p < 0.05$, and $****p < 0.0001$. The presence of outliers was analyzed by Grubb's test (alpha = 0.05) using GraphPad online outlier calculator. Outliers were removed from the dataset. Data are represented as the mean ± SD of three independent repeats.

Supporting Information

Supporting Information is available from the Wiley Online Library or from the author.

Acknowledgements

M.A.R.D., X.Q., C.A., and T.F.M. contributed equally to this work. This project was supported by a Carlsberg Foundation Distinguished Associate Professor Fellowship (B.S. CF16-0233), the Lundbeck Foundation, the Sino-Danish Center (SDC) for Education and Research, and the European Research Council (ERC) under the European Union's Horizon 2020 research and innovation program (grant agreement No. 818890).

Conflict of Interest

The authors declare no conflict of interest.

Data Availability Statement

The raw/processed data required to reproduce these findings are available to download from https://osf.io/9r3n5/?view_only=8112c8ced0e64878bc323c79eae3f859.

Keywords

cell internalization, locomotion in cell media, nanomotors, PEG, pH-responsive linkers

Received: July 8, 2022
Revised: September 14, 2022
Published online: October 10, 2022

[1] G. Tezel, S. S. Timur, F. Kuralay, R. N. Gürsoy, K. Ulubayram, L. Öner, H. Eroğlu, *J. Drug Targeting* **2020**, *29*, 29.
[2] H. Yuan, X. Liu, L. Wang, X. Ma, *Bioact. Mater.* **2021**, *6*, 1727.
[3] M. Yan, L. Xie, J. Tang, K. Liang, Y. Mei, B. Kong, *Chem. Mater.* **2021**, *33*, 3022.
[4] M. Fernández-Medina, M. A. Ramos-Docampo, O. Hovorka, V. Salgueiriño, B. Städler, *Adv. Funct. Mater.* **2020**, *30*, 1908283.
[5] Y. Wu, Z. Song, G. Deng, K. Jiang, H. Wang, X. Zhang, H. Han, *Small* **2021**, *17*, 2006877.
[6] P. L. Venugopalan, B. Esteban-Fernández De Ávila, M. Pal, A. Ghosh, J. Wang, *ACS Nano* **2020**, *14*, 9423.
[7] W. Liu, W. Wang, X. Dong, Y. Sun, *ACS Appl. Mater. Interfaces* **2020**, *12*, 12618.
[8] J. Wu, S. Ma, M. Li, X. Hu, N. Jiao, S. Tung, L. Liu, *ACS Appl. Mater. Interfaces* **2021**, *13*, 31514.
[9] Y. Shen, W. Zhang, G. Li, P. Ning, Z. Li, H. Chen, X. Wei, X. Pan, Y. Qin, B. He, Z. Yu, Y. Cheng, *ACS Nano* **2021**, *15*, 20020.
[10] J. Wang, X. Liu, Y. Qi, Z. Liu, Y. Cai, R. Dong, *Chem. Eng. J.* **2021**, *416*, 129091.
[11] A. C. Hortelão, T. Patiño, A. Perez-Jiménez, À. Blanco, S. Sánchez, *Adv. Funct. Mater.* **2018**, *28*, 1705086.
[12] Y. Tu, F. Peng, A. A. M. Andre, Y. Men, M. Srinivas, D. A. Wilson, *ACS Nano* **2017**, *11*, 1957.
[13] J. Sun, M. Mathesh, W. Li, D. A. Wilson, *ACS Nano* **2019**, *13*, 10191.
[14] A. Llopis-Lorente, A. Garciá-Fernández, N. Murillo-Cremaes, A. C. Hortelaõ, T. Patinõ, R. Villalonga, F. Sancenón, R. Martínez-Máñez, S. Sánchez, *ACS Nano* **2019**, *13*, 12171.
[15] M. Mathesh, J. Sun, F. Van Der Sandt, D. A. Wilson, *Nanoscale* **2020**, *12*, 22495.
[16] M. A. Ramos-Docampo, M. Fernández-Medina, E. Taipaleenmäki, O. Hovorka, V. Salgueirinõ, B. Städler, *ACS Nano* **2019**, *13*, 12192.
[17] A. C. Hortelao, R. Carrascosa, N. Murillo-Cremaes, T. Patino, S. Sánchez, *ACS Nano* **2019**, *13*, 429.
[18] J. Ou, H. Tian, J. Wu, J. Gao, J. Jiang, K. Liu, S. Wang, F. Wang, F. Tong, Y. Ye, L. Liu, B. Chen, X. Ma, X. Chen, F. Peng, Y. Tu, *ACS Appl. Mater. Interfaces* **2021**, *13*, 38050.
[19] B. D. Monnery, *Biomacromolecules* **2021**, *22*, 4060.
[20] Z. Liao, L. Tu, X. Li, X. J. Liang, S. Huo, *Nanoscale* **2021**, *13*, 18912.
[21] H. Yokoo, M. Oba, S. Uchida, *Pharmaceutics* **2022**, *14*, 78.
[22] J. Shinn, N. Kwon, S. A. Lee, Y. Lee, *J. Pharm. Invest.* **2022**, *52*, 427.
[23] X. Li, E. C. Montague, A. Pollinzi, A. Lofts, T. Hoare, *Small* **2022**, *18*, 110758.
[24] M. Gisbert-Garzaran, D. Lozano, K. Matsumoto, A. Komatsu, M. Manzano, F. Tamanoi, M. Vallet-Regi, *ACS Appl. Mater. Interfaces* **2021**, *13*, 9656.
[25] C. Xu, S. Wang, H. Wang, K. Liu, S. Zhang, B. Chen, H. Liu, F. Tong, F. Peng, Y. Tu, Y. Li, *Nano Lett.* **2021**, *21*, 1982.
[26] S. Bazban-Shotorbani, M. M. Hasani-Sadrabadi, A. Karkhaneh, V. Serpooshan, K. I. Jacob, A. Moshaverinia, M. Mahmoudi, *J. Controlled Release* **2017**, *253*, 46.
[27] S. Zhuo, F. Zhang, J. Yu, X. Zhang, G. Yang, X. Liu, *Molecules* **2020**, *25*, 5649.
[28] Y. Tao, X. Li, Z. Wu, C. Chen, K. Tan, M. Wan, M. Zhou, C. Mao, *J. Colloid Interface Sci.* **2021**, *611*, 61.
[29] X. Xu, J. D. Flores, C. L. McCormick, *Macromolecules* **2011**, *44*, 1327.
[30] C. Yuan, B. Hong, Y. Chang, J. Mao, Y. Li, Y. Xu, B. Zeng, W. Luo, J. F. Gérard, L. Dai, *ACS Appl. Mater. Interfaces* **2017**, *9*, 14700.
[31] J. Hatai, C. Hirschhäuser, J. Niemeyer, C. Schmuck, *ACS Appl. Mater. Interfaces* **2020**, *12*, 2107.
[32] Y. Li, Q. N. Bui, L. T. M. Duy, H. Y. Yang, D. S. Lee, *Biomacromolecules* **2018**, *19*, 2062.
[33] X. Hu, A. M. Jazani, J. K. Oh, *Polymer* **2021**, *230*, 124024.
[34] S. E. Lehman, J. M. McCracken, L. A. Miller, S. Jayalath, R. G. Nuzzo, *Adv. Healthcare Mater.* **2021**, *10*, 2100126.
[35] C. Wang, S. S. Rubakhin, M. J. Enright, J. V. Sweedler, R. G. Nuzzo, *Adv. Funct. Mater.* **2021**, *31*, 2010246.
[36] E. Brodszkij, M. J. Hviid, C. Ade, P. S. Schattling, M. Burmeister, S. Szilagyi, N. Gal, C. Zhu, X. Han, B. Städler, *Polym. Chem.* **2019**, *10*, 5992.
[37] P. De Dios Andres, I. N. Westensee, E. Brodszkij, M. A. Ramos-Docampo, N. Gal, B. Städler, *Biomacromolecules* **2021**, *22*, 3860.
[38] C. Ade, X. Qian, E. Brodszkij, P. De Dios Andres, J. Spanjers, I. N. Westensee, B. Städler, *Biomacromolecules* **2022**, *23*, 1052.
[39] T. Thanh, H. Thi, E. H. Pilkington, D. H. Nguyen, J. S. Lee, *Polymers* **2020**, *12*, 298.
[40] J. Zhu, *Biomaterials* **2010**, *31*, 4639.
[41] P. Schattling, B. Thingholm, B. Städler, *Chem. Mater.* **2015**, *27*, 7412.
[42] A. Nsamela, P. Sharan, A. Garcia-Zintzun, S. Heckel, P. Chattopadhyay, L. Wang, M. Wittmann, T. Gemming, J. Saenz, J. Simmchen, *ChemNanoMat* **2021**, *7*, 1042.
[43] W. Stöber, A. Fink, *J. Colloid Interface Sci.* **1968**, *26*, 62.
[44] J. Y. Tinevez, N. Perry, J. Schindelin, G. M. Hoopes, G. D. Reynolds, E. Laplantine, S. Y. Bednarek, S. L. Shorte, K. W. Eliceiri, *Methods* **2017**, *115*, 80.
[45] N. Tarantino, J.-Y. Tinevez, E. F. Crowell, B. Boisson, R. Henriques, M. Mhlanga, F. Agou, a. Israel, E. Laplantine, *J. Cell Biol.* **2014**, *204*, 231.